



Subglacial landscape formation and sediment discharge: relating basal conditions to bedform dimensions and properties at Rutford Ice Stream, West Antarctica

REBECCA SCHLEGEL , LUCAS K. ZOET, ADAM D. BOOTH, ANDREW M. SMITH, ROGER A. CLARK AND ALEX M. BRISBOURNE 

BOREAS



Schlegel, R., Zoet, L. K., Booth, A. D., Smith, A. M., Clark, R. A. & Brisbourne, A. M.: Subglacial landscape formation and sediment discharge: relating basal conditions to bedform dimensions and properties at Rutford Ice Stream, West Antarctica. *Boreas*. <https://doi.org/10.1111/bor.70002>. ISSN 0300-9483.

Basal conditions that facilitate fast ice flow are still poorly understood and their parameterization in ice-flow models results in high uncertainties in ice-flow and consequent sea-level rise projections. Direct observations of basal conditions beneath modern ice streams are limited due to the inaccessibility of the bed. One approach to understanding basal conditions is through investigating the basal landscape of ice streams and glaciers, which has been shaped by ice flow over the underlying substrate. Bedform variation together with observations of ice-flow properties can reveal glaciological and geological conditions present during bedform formation. Here we map the subglacial landscape and identify basal conditions of Rutford Ice Stream (West Antarctica) using different visualization techniques on novel high-resolution 3D radar data. This novel approach highlights small-scale features and details of bedforms that would otherwise be invisible in conventional radar grids. Our data reveal bedforms of <300 m in length, surrounded by bedforms of >10 km in length. We correlate variations in bedform dimensions and spacing to different glaciological and geological factors. We find no significant correlation between local (<3 × 3 km) variations in bedform dimensions and variations in ice-flow speed and (surface or basal) topography. We present a new model of subglacial sediment discharge, which proposes that variations in bedform dimensions are primarily driven by spatial variation in sediment properties and effective pressure. This work highlights the small-scale spatial variability of basal conditions and its implications for basal slip. This is critical for more reliable parameterization of basal friction of ice streams in numerical models.

Rebecca Schlegel (rebecca.schlegel@uni-tuebingen.de), Department for Geoscience, University of Tübingen, Tübingen 72070, Germany, British Antarctic Survey, Natural Environment Research Council, Cambridge CB3 0ET, UK and Glaciology Group, Department of Geography, Swansea University, Swansea SA2 8PP, UK; Lucas K. Zoet, Department of Geoscience, University of Wisconsin–Madison, Madison 53706-1600, USA; Adam D. Booth and Roger A. Clark, School of Earth and Environment, University of Leeds, Leeds LS2 9JT, UK; Andrew M. Smith and Alex M. Brisbourne, British Antarctic Survey, Natural Environment Research Council, Cambridge CB3 0ET, UK; received 7th November 2024, accepted 24th February 2025.

Friction at the base of marine-terminating glaciers and ice streams controls ice-flow speed and ice discharge into oceans (Zoet & Iverson 2020; Hudson *et al.* 2023). Properties such as yield stress and pore-water pressure within the subglacial sediment influence the friction provided by the bed upon the overlying ice. In ice-flow models, basal friction is parametrized and estimated from inversions of ice-flow speed and ice geometry (Joughin *et al.* 2019), but knowledge of the frictional slip response is needed to accurately predict future sliding speeds. Various studies have demonstrated the strong dependence of ice discharge estimates on the chosen slip law and its dependent parameters (Gillet-Chaulet *et al.* 2016; Nias *et al.* 2018; Brondex *et al.* 2019; Joughin *et al.* 2019). Uncertainties when determining or estimating these parameters result in high uncertainties in predictions of ice dynamics, and thus of the consequent sea-level rise (Ritz *et al.* 2015; Bamber *et al.* 2019; Fox-Kemper *et al.* 2023).

In-situ observations of basal conditions (e.g. through boreholes) that can characterize basal properties and dynamics are few in number, but information about the physical properties of the ice-bed interface is also

encoded in the subglacial landscape. Elongated bedforms are considered a by-product of fast ice flow (Clark 1993; Stokes & Clark 2001; Johnson *et al.* 2010; Spagnolo *et al.* 2014; Clark *et al.* 2018; Finlayson *et al.* 2019; Zoet *et al.* 2021). Mapping of variations in bedform elongation ratio (length vs. width ratio), and analysis of factors causing these variations, allows insights into basal properties that facilitate fast ice flow.

Observations in the palaeo-record (Clark 1993; Stokes & Clark 2002; Zoet *et al.* 2021), from beneath a modern ice stream (Clyne *et al.* 2020; Holschuh *et al.* 2020) and from laboratory experiments (Zoet & Iverson 2020; Hansen & Zoet 2022) suggest various potential influences on bedform length. Various factors have been proposed, including both glaciological (i.e. ice-flow velocity, strain rate, time integrated velocity, ice surface slope, basal topography, and effective pressure) and geological (i.e. stiffness of the bed, properties of the sediment and basal hydrology) factors. The increasing amount of geophysical data available for various modern ice streams allows the direct correlation of bedform dimensions with glaciological and geological factors (Holschuh *et al.* 2020).

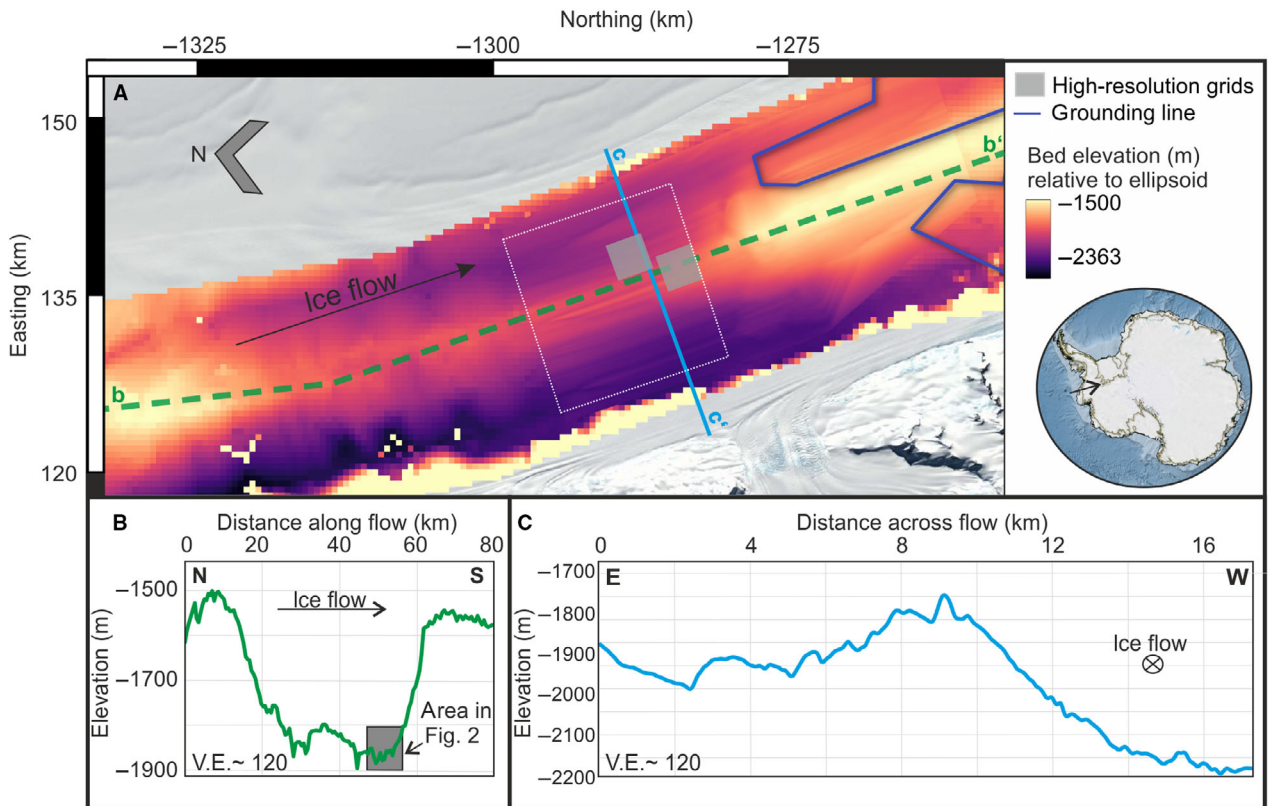


Fig. 1. Bed topography beneath RIS from airborne (Corr 2020) and ground-based radar data (King *et al.* 2009; Schlegel *et al.* 2022). A. Elevation relative to WGS84 ellipsoid, the position of the grounding line from satellite observations (1991–2003, Bindshadler *et al.* 2011) is shown in blue. The area studied here is marked by the grey-filled squares. B. Bed elevation along the green dashed line in A. C. Bed elevation across flow (along the blue solid line in A). The background shows the LIMA Landsat high-resolution virtual mosaic (15 m). The white box in A marks the location of data shown in Fig. 2.

In this paper, we present a new approach to analysing bedforms and constraining their dimensions in the modern glaciated environment. These observations are combined with a novel model of sediment discharge. Spatial variations in sediment discharge are then used to explain variations in bedform dimensions, such that low sediment discharge can be found in areas of smaller bedforms and vice versa. For dimensional constraint, we image bedform geometry beyond the capabilities of previous radar data using radar surveys acquired at sufficiently close 2D profile spacing to be compliant with processing in a 3D manner (Schlegel *et al.* 2024), which improves imaging of the 3D basal topography, and an extended suite of interpretative tools, that allow metre-scale topographic variations to be mapped and interpreted. These geophysical observations are further used as the input for our sediment discharge model. This model allows first-order controls on bedform dimensions beneath Rutford Ice Stream to be identified.

Location and data

Bedforms and basal conditions beneath the Rutford Ice Stream (RIS) in West Antarctica (Fig. 1) have been studied for over 40 years (Doake *et al.* 1987), lately as part of

the BEAMISH project (Smith *et al.* 2021). The bedforms investigated here (grey boxes in Fig. 1A) lie approximately 40–50 km upstream of the grounding line. Figure 2 shows the bed topography in the study area as imaged in previous studies using ground-based radar data (Schlegel *et al.* 2022, 2024). In this region, surface ice flows at $\sim 380 \text{ m a}^{-1}$ (Murray *et al.* 2007). The bed in this area consists of soft material, where basal motion is likely dominated by basal deformation, and harder material, where the dominant motion mechanism is assumed to be basal sliding (e.g. Smith 1997; Smith & Murray 2009). King *et al.* (2009) mapped the extent of both materials and defined a boundary between them (red dashed line in Fig. 2), which partly coincides with a topographic change.

Bedforms mapped in previous studies

Consistent with observations in the palaeo-record (Stokes 2018), bedforms beneath RIS show a down-flow transition: bedforms in the onset region (interpreted as ribs), are shorter ($< 2 \text{ km}$ length) compared to more elongated bedforms (interpreted as drumlins) further downstream (King *et al.* 2007). The increased elongation of bedforms along flow correlates with an increase in ice-

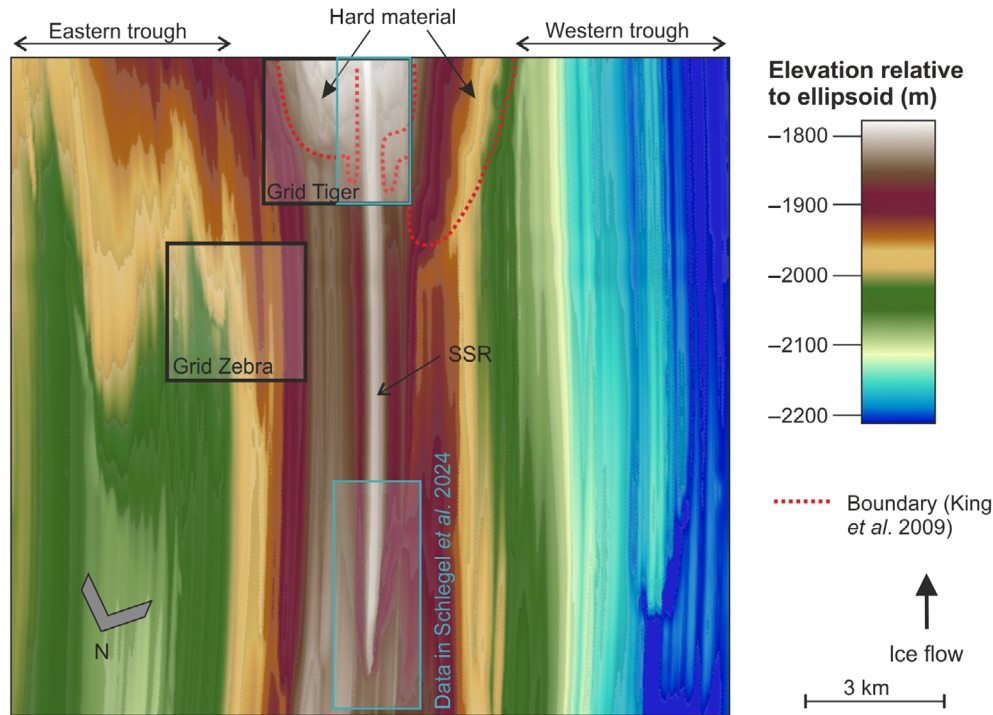


Fig. 2. Bed elevation beneath RIS in plan view, referenced to the WGS84 ellipsoid. For the location of these data see white box in Fig. 1. Black and cyan boxes mark the location of 3D high-resolution radar data. The red dashed lines mark the boundary between soft (deforming) and stiff (non-deforming) subglacial material (King *et al.* 2009). 3D radar data in the cyan boxes are analysed in Schlegel *et al.* (2024).

flow speed from 70 to 125 m a⁻¹ (King *et al.* 2007). The steep upstream end of these drumlins is interpreted to consist of hard material, with a soft tail. Further downstream, where ice flows at 380 m a⁻¹, previous studies imaged the bed topography using 2D-migrated radar lines spaced at 500-m lateral separation and orientated perpendicular to the ice flow (King *et al.* 2016; Schlegel *et al.* 2022), highlighting that the bed is composed of numerous bedforms that, in places, are over 14 km long (Fig. 2). Seismic acoustic impedance and the observation of active lengthening of a bedform between survey periods suggest that bedforms are depositional features that consist of soft sediment (Smith *et al.* 2007), indicating that sediment discharge through the bed is responsible for their development. Similarly to the bedforms in the onset region, some bedforms here are composed of a steep and hard upstream portion with a softer and more water-saturated tail along their crest (Murray *et al.* 2008; Schlegel *et al.* 2022, 2024). However, extensive analysis of radar and seismic data along the bedform referred to as the Smith Subglacial Ridge (SSR) implies that the upstream end of this specific feature lacks a hard outcrop that would act as a seed point (Schlegel *et al.* 2024).

New data for bedform mapping

As part of the BEAMISH project, areas of interest were identified and imaged based on the bed topography

derived in previous studies (Fig. 2). Areas investigated focussed on the previously identified boundary, a topographic step that was not aligned in flow direction and the upstream end of a prominent bedform (Schlegel *et al.* 2024). 3D radar data over these areas were acquired in 2017/2018 using the DELORES system (King *et al.* 2007), a pulse radar with a centre frequency of approximately 3.5 MHz. In total, three grids of 3 × 3 km were acquired over 25 days. Each grid consists of 151 3-km-long parallel profiles, separated by 20 m and orientated approximately perpendicular to ice flow. The resulting sampling is compliant with 3D migration (Schlegel *et al.* 2024) and allows detailed 3D imaging of complex structures (Grasmueck *et al.* 2005; Booth *et al.* 2008; Koyan *et al.* 2021). Data within two of these grids (Tiger and Zebra, Fig. 2) are presented here. Grid Tiger is located on the topographic high, in the area where previous studies (Smith 1997; King *et al.* 2009; Smith & Murray 2009) identified a geological boundary (Fig. 2). Grid Zebra is located northeast of Grid Tiger towards the eastern trough, but is not located over the deepest part of the trough. The third acquired grid (referred to as the upstream grid) as well as the western part of Grid Tiger were described and analysed in Schlegel *et al.* (2024).

Radar data in Grids Tiger and Zebra were processed as described in Schlegel *et al.* (2024), including data regularization, frequency filtering, correction for geometric

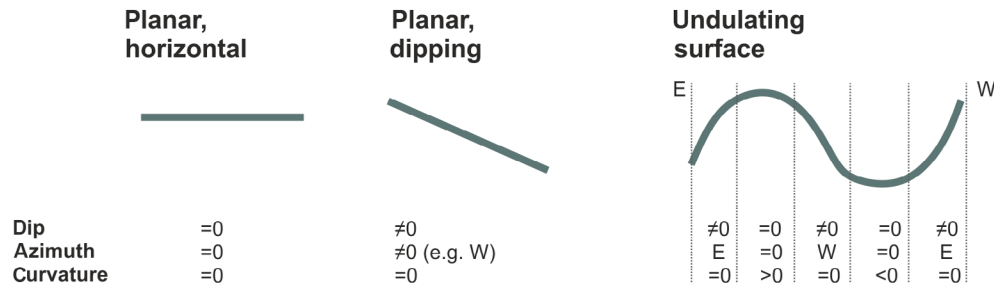


Fig. 3. Relationship between different structural attributes: dip, dip azimuth and curvature. Here the curvature is chosen to illustrate the cardinal points towards which the slope is dipping. 'E' and 'W' are east and west, respectively, in this example we show a 2D surface that is invariant in the north–south direction.

spreading and englacial attenuation losses (using the depth-averaged attenuation rate of $\sim 20 \text{ dB km}^{-1}$ in this area found by Schlegel *et al.* (2022)). Following this, a 3D Kirchhoff time migration was applied using a migration speed of 0.168 m ns^{-1} with migration aperture limited to a maximum allowed dip angle of 30° and stretch mute of 15%. This processing delivered a theoretical horizontal resolution of 24 m (Schlegel *et al.* 2024) and a vertical precision better than 3 m (King 2020). After processing the 3D volumes, ice thickness was evaluated using the first arrivals of the airwave and the bed reflection. The bed reflection was picked on the first coherent arrival near the expected two-way travel time of $\sim 25\,000 \text{ ns}$ for 2100-m ice thickness using a semi-automated routine in Petrel (Schlumberger Software). Conversion of travel-time to depth assumed a radar speed of 0.168 m ns^{-1} , and the resulting horizon was interpolated onto a surface with $65 \times 20 \text{ m}$ grid cell dimensions using a convergent interpolation algorithm in Petrel. The data acquisition and 3D processing of the radar data allow the bed to be sampled to its optimal theoretical limit (Schlegel *et al.* 2024). Because of this dense sampling, the interpolation of bed picks is used primarily for illustrative reasons and not to fill data gaps, which increases the interpretative potential of this data set compared to other sparsely sampled data (King *et al.* 2009; Bingham *et al.* 2017).

Bedform mapping and correlation with ice flow

Attribute analysis

An attribute of a data set is defined as some characteristic of the recorded data that is a function of the physical properties and geometry of the subsurface (Chopra & Marfurt 2007; Mohebian *et al.* 2018). Originally developed for reflection seismology (Taner 2001; Chopra & Marfurt 2005, 2007), the calculation of data attributes provides quantitative, objective and visual information on features such as small-scale structures and irregularities (Zhao *et al.* 2016).

Following Taner (2001), we segregate attributes into (i) structural, for attributes solely dependent on geo-

metric aspects of a topographic horizon (here: the bed topography), and (ii) physical, for attributes based on waveform characteristics along a reflection (here: individual traces along the bed reflection). We briefly introduce the attributes that have delivered the most information for the radar data presented here.

Structural attributes. – Structural attributes highlight the local deviation of topography, in our case the bed topography compared to some reference surface. We use structural attributes of dip, dip azimuth and curvature (Fig. 3). The attributes of dip and dip azimuth show structural trends compared to a horizontal plane. The curvature attribute describes the deformation or bend of the bed, relative to a planar horizon. As shown in Fig. 3, a horizontal planar surface will have curvature, dip and dip azimuth of zero; a dipping planar surface has zero curvature and non-zero dip and dip azimuth. An undulating surface shows systematic variation in all three attributes, which can be combined to uniquely constrain its geometry.

Physical attributes. – Physical attributes describe waveform characteristics such as amplitude, which can be used to identify changes in the physical properties of the material on either side of an interface (e.g. Taner *et al.* 1979; Zhao *et al.* 2016; Delf *et al.* 2020). In the case of the ice-bed reflection of an ice stream, changes in the amplitude can indicate variations in the water content of the basal sediment (Murray *et al.* 2008; Ashmore & Bingham 2014; Chu *et al.* 2016) and/or identify the location of subglacial lakes and channels (Siegert & Ridley 1998; Carter *et al.* 2007; Wright *et al.* 2014).

As detailed in Schlegel *et al.* (2024), the square root of the sum-of-squared-amplitudes, referred to as bed-reflection voltage (BRV), is a proxy for the reflection amplitude coefficient. To assign BRV to absolute bed properties and porosities, a calibration of BRV at sites of known properties is applied. We refer to the calibrated (thus absolute) BRV as reflectivity, which is unitless. Previous studies on RIS (Schlegel *et al.* 2022, 2024) calibrated the BRV using seismic reflection data to allow

the assignment of sediment porosity ranges to values of BRV. As data were acquired with the same radar system and overlap with these previous studies, we adopt this same calibration here. Following Schlegel *et al.* (2022), we assign reflectivity values of above 1.8 to represent sediment with porosity above 50%. Sediment in the range of 30–50% porosity is assumed to be deforming, which would correspond to reflectivity values of 0.6–1.8. Areas with lower reflectivity are assumed to represent sediment with porosity less than 30%, where the bed is less likely to be deforming.

Identification and mapping of bedforms

Topographic features that are continuous over several radar lines were identified using patterns in inferred elevation, dip, dip azimuth and curvature. We only investigate features that appear within the actual radargrams to ensure that any interpolation artefacts are not interpreted as bedforms. The dimensions of bedforms were mapped from the elevation measured from the radargrams. Owing to the spatial sampling of the basal topography, bedform length can be identified with an uncertainty of ± 20 m, and width with an uncertainty of ± 12 m.

After identifying the features, we assign appropriate nomenclature to them. In Grid Zebra, we categorize bedforms into two types: continuous bedforms (Bc) if they exist over the full length of the grid, therefore bedforms of at least 3 km length, and interrupted bedforms (Bi), if they terminate or emerge within the grid, therefore bedform length of less than 3 km visible in that grid. Within Grid Tiger only the SSR bedform is continuous. Apart from the SSR, we differentiate between bedforms located upstream and downstream of the boundary (King *et al.* 2009), labelled Bu and Bd, respectively. Note that bedforms Bu terminate at the boundary and bedforms Bd emerge downstream of the boundary.

Correlation with glaciological parameters

We correlated the various bedform dimensions with different glaciological parameters to identify their influence on bedforms. We chose the following data sets:

- Surface flow speed: speed data at 240-m resolution from 1985 to 2018 were derived from Landsat 4, 5, 7 and 8 imagery using the auto-RIFT feature tracking processing chain (Gardner *et al.* 2018), provided by the NASA Inter-mission Time Series of Land Ice Velocity and Elevation (ITS LIVE) project (Gardner *et al.* 2019).
- Surface elevation, slope and azimuth acquired from 2009 until 2021: extracted from the Reference Elevation Model of Antarctica (REMA) reported to be at 2-m spatial resolution (Howat *et al.* 2022).

Sediment discharge model

Background from previous laboratory experiments

Until now, no simple link between the individual geological and glaciological factors and the dimensions of the subglacial bedforms has been identified. Here we propose a new model that predicts sediment discharge (in $\text{m}^3 \text{a}^{-1}$), outputs of which are then compared to the measured variations in bedforms. This new model is based on independent variables such as: u_t – the speed at which the bed begins to deform; N – the basal effective pressure; and u_b – the slip speed of the ice (equal to the ice-flow speed at the base).

Laboratory experiments of Zoet and Iverson (2020) demonstrated that sediment deformation will not begin until the shear traction (imposed on the sediment surface by the overriding ice) meets the yield strength of the till. As the ice is viscous and the sediment is a granular material with a finite strength, the value at which the threshold is met corresponds to a specific slip speed, u_t (m s^{-1}). u_t depends on several factors related to intrinsic properties of the sediment (e.g. bearing capacity, grain sizes; see Zoet & Iverson (2020) for the full expression) and the basal effective pressure N (Pa). The relation between N and u_t can be expressed as

$$u_t = NC_t, \quad (1)$$

where C_t ($\text{s m}^2 \text{kg}^{-1}$) is a constant depending on the physical properties of the ice and till.

Hansen & Zoet (2022) showed that sediment discharge is nearly linearly proportional to the slip speed of the overriding ice, assuming other factors to be constant. This near-linearity occurs because of the coupling of the viscous ice to the granular sediment layer beneath, and therefore the stress exerted on the sediment is controlled by the fluidity of the ice. Analysing sediment discharge and the formation of drumlins beneath the Laurentide Ice Sheet, Zoet *et al.* (2021) confirmed this near-linear proportionality. However, sediment discharge, Q , only occurs once the basal ice slip velocity u_b exceeds the transition velocity, u_t , from Equation 1. Thus, no sediment deformation, and hence sediment discharge, can occur at $u_b < u_t$. We therefore define Q as

$$Q = T_{sb} \max(0, u_b - u_t), \quad (2)$$

where T_{sb} is an expression for the thickness (depth) of the deforming sediment band. Hansen & Zoet (2022) showed that the thickness of the deforming sediment band, T_{sb} , is dependent on N via a nonmonotonic relationship. This means that at low effective pressure T_{sb} increases with increasing effective pressure until an inflection pressure is reached, whereupon T_{sb} decreases with increasing effective pressure (Fig. S1). The mecha-

nistic reason for this pattern stems from the development of force chains within the sediment as the effective pressure changes. Such a nonmonotonic expression can be expressed simply as

$$T_{sb} = C_1 \frac{N}{C_2 + N^2} \quad (3)$$

where C_1 and C_2 are constants related to the scaling of the nonmonotonic function to experiments and depend on the physical properties of the till. By fitting Equation 3 to data in Hansen & Zoet (2022), C_1 and C_2 can be estimated. Doing so, it was found that $C_1 = 1.5 \times 10^3$ (kg s^{-2}) and $C_2 = 2 \times 10^9$ (Pa^2) provided an RMS misfit of 0.01 to the experimental data (Fig. S1). C_1 in Equation 1 can be taken directly from Zoet & Iverson (2020) where it was found to range from 1.1×10^{-11} to 5.3×10^{-11} ($\text{s m}^2 \text{kg}^{-1}$), for till with and without clasts, respectively (note this was the same sediment as used in Hansen & Zoet 2022).

New proposed model for sediment discharge

Combining Equations 2 and 3 and calculating u_t in Equation 1 provides the equation

$$Q = C_1 \frac{N}{C_2 + N^2} \max(0, u_b - u_t), \quad (4)$$

a general expression for subglacial sediment discharge, Q , that honours the physical mechanisms that drive sediment deformation. This equation states that no sediment will be discharged for $u_b < u_t$. u_t has a dependence on N and sediment properties. The occurrence of stiff sediment, either because sediment has been consolidated (low porosity) or due to its inherent material properties, or because N values are high, may result in an elevated u_t . As shown in Zoet *et al.* (2021) an elevated u_t can inhibit deformation of the underlying bed. Following Zoet *et al.* (2021) and Boulton (1987) we assume a lower sediment discharge rate, thus less sediment being moved, to result in shorter and less-pronounced bedforms.

With Equation 4, a general sediment discharge, Q , for a unit width (e.g. 1 m), can be estimated in different areas depending on variations in sliding speed, effective pressure and sediment properties. This new expression enables us to infer information about slip-facilitating processes and how they vary spatially from geophysical and glaciological observations. For example, when $u_b < u_t$ basal motion occurs primarily via sliding atop the till but when $u_b > u_t$ basal motion results largely from deformation of the bed material thus providing insight into the slip mechanics (Zoet & Iverson 2020; Hansen & Zoet 2022).

The model and constants in Equation 4 were derived from relations observed in laboratory experiments using representative tills, some with large clasts and some without. As much of the sediment in Antarctica is derived from marine muds (Tulaczyk *et al.* 1998), values representing a lack of clasts are likely more appropriate. For the calculation of sediment discharge beneath the RIS we can use measurements of surface ice-flow speed from GPS data (Murray *et al.* 2007) and effective pressure measured at the bed (Smith *et al.* 2021). A drilling campaign in 2018/2019 accessed the bed beneath RIS in two locations. Basal effective pressure of 0.168 and 0.193 MPa was measured upstream of Grid Tiger and 0.204 MPa downstream of the boundary in Grid Tiger (Smith *et al.* 2021). We calculate spatial variation in sediment discharge Q using this range of values of effective pressure, an ice-flow speed of 380 m a^{-1} (Murray *et al.* 2007) and the previous constants generated from the laboratory experiments.

Bedforms, bed properties and sediment discharge beneath Rutford Ice Stream

Bed topography and reflectivity

Bed elevation is displayed in plan (Fig. 4, top) and isometric (Fig. 4, bottom) view. Most of the bed is nearly flat, with 83% (Zebra) and 91% (Tiger) of the topography dipping at less than 10° (dip attributes in Fig. 5A, B). Both grids contain structures aligned in the ice-flow direction, visible when looking at the variation in cross-flow dip (Fig. 5A, B). In Grid Zebra, the dip varies on a small (50–100 m) spatial scale across flow (visible as the yellow-red-yellow pattern representing 0 to 15° dip in Fig. 5A), and shows a strong correlation along flow, except for the area named ‘interruption’ (red dashed line). The terminology ‘interruption’ is introduced to distinguish this feature from the ‘boundary’ identified in Grid Tiger, which was mapped in previous studies based on variations in basal properties and topography. The variation in cross-flow dip in Grid Zebra is roughly the same both up- and downstream of the interruption. Similarly, the dip azimuth (Fig. 5C, blue-yellow pattern) and curvature (Fig. 5E, red-blue pattern) attributes highlight the small-scale variation across flow and strong correlation along flow.

In Grid Tiger a spatial coherency of structural attributes along flow is visible until the boundary is reached (Fig. 5B, D, F). Upstream of the boundary, the spatial variation in dip and dip azimuth across flow varies on a larger scale (200–400 m, Fig. 5B, D) when compared to Grid Zebra (50–100 m, Fig. 5A, C). Downstream of the boundary the topography occasionally aligns well with the flow direction over a distance of 200–300 m; there are also alignments $\sim 30^\circ$ east of flow direction (black solid lines, Fig. 5J), referred to as cross-cutting

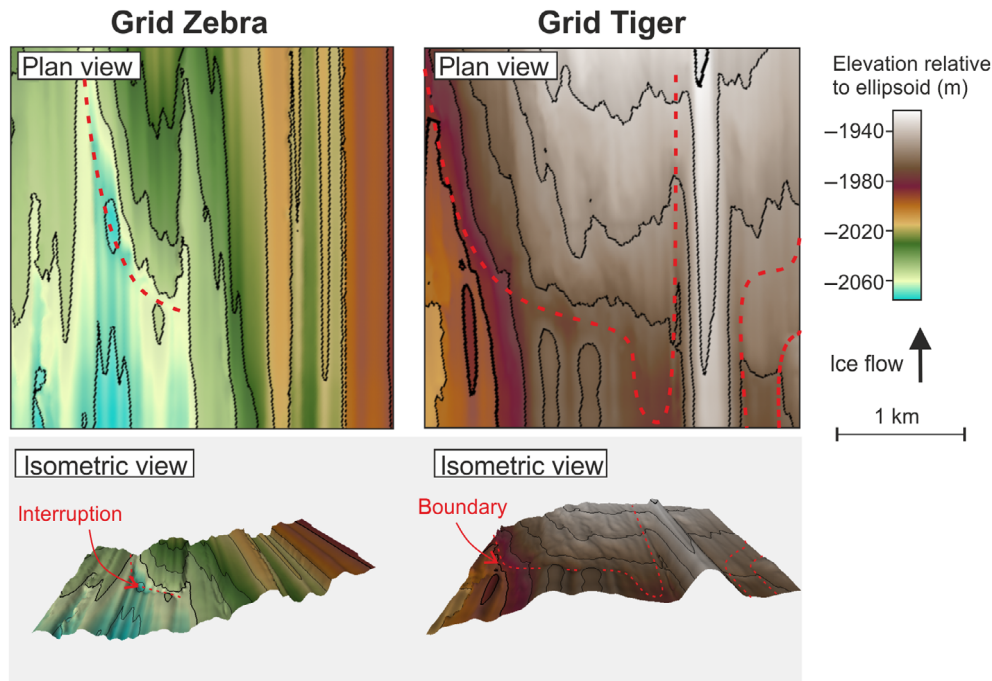


Fig. 4. Elevation of the bed topography within Grids Zebra and Tiger relative to the WGS84 ellipsoid. Top panel shows bed elevation in plan view, and bottom panel in isometric view. The transition from soft to hard sediment in Grid Tiger, identified by King *et al.* (2009), is referred to as a boundary, whereas the topographic step identified in Grid Zebra is referred to as an interruption. The isometric view (bottom panel) shows the topography as viewed from within the ice, at 5 \times vertical exaggeration.

features. No such cross-cutting features are identified in Grid Zebra.

The pattern of the bed reflectivity (Fig. 5G, H) shows a similar trend to those in the structural attributes: the spatial scale of variation across flow varies between the grids. In Grid Zebra we find a similar pattern of reflectivity up- and downstream of the interruption, whilst the pattern changes significantly in Grid Tiger up- and downstream of the boundary. Downstream of the boundary, reflectivity is low (most areas <0.5). Within the area of identified hard material, higher reflectivity (~ 0.75 – 1) values seem occasionally to be aligned in the flow direction. Cross-cutting features identified from structural attributes show low reflectivity (<0.5).

Bedform dimensions and reflectivity

Figure 5I, J shows the bed topography with bedforms labelled and crests marked by yellow dashed lines. Dimensions of the bedforms can be found in Table 1. Some bedforms (Bc1–6) in Grid Zebra are continuous throughout the length of the grid (bedform length ≥ 3 km), except for bedforms in the location of the interruption (labelled Bi1–10). The width of continuous bedforms in Grid Zebra varies between 95 and 230 m (Fig. 6). Interrupted bedforms are 45–120 m wide and 1–6 m high. The height and width of bedforms up- and downstream of the interruption are in the same range, and have

roughly the same spacing between them; however, they are shifted relative to each other along the flow, such that bedform crests do not align along the flow direction up- and downstream of the interruption. Bedform downstream ends in both grids are distinct with a continuous topographic depression surrounding them (outline or depression marked in yellow in Fig. 7). Where bedforms terminate in Grid Zebra, a drop in topography of 10 m is visible (purple line in Fig. 6).

Within Grid Tiger, only one bedform, the SSR, is continuous along the length of the grid (bedform length ≥ 3 km); other bedforms (e.g. Bu1–5) terminate at the boundary. The red line in Fig. 8 shows the bed elevation along and beyond bedform Bu2, where a topographic drop of 15 m is visible. Small features aligned in the flow direction downstream of the boundary are interpreted to be small bedforms (Bd1–9) of 200–300 m lengths. Bedform widths and heights are 100–300 m and 3–12 m upstream of the boundary (Fig. 8) and, downstream, 60–150 m and 1–4 m, respectively. Bedforms upstream of the boundary are more pronounced, highlighted by flanks dipping at up to 20° for the SSR and 15° for Bu1. In the area of the hard material, the topographic relief of bedforms is smaller and flanks dip at $<10^\circ$.

Bedforms in both grids show stronger reflectivity compared to the surroundings (Fig. 5G, H). No variation in reflectivity can be seen along the crest of continuous bedforms in either grid. Small bedforms in the hard

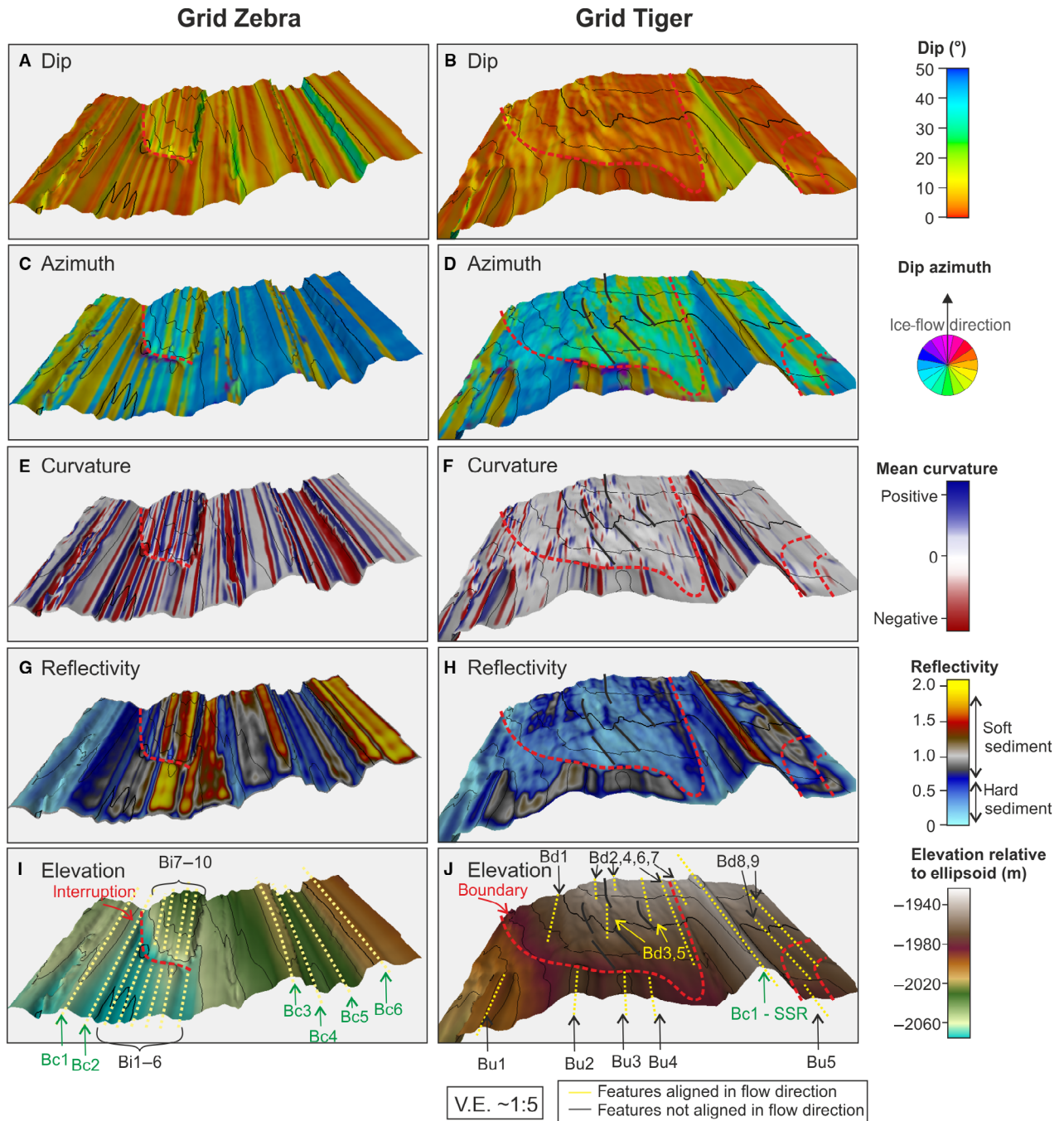


Fig. 5. Basal topography in Grid Zebra (left) and Grid Tiger (right). Top panel: dip of the topography, second panel: azimuth, third panel: curvature, fourth panel: reflectivity and lowest panel: elevation of the topography. The azimuth highlights areas dipping in the flow direction in pink. Topography dipping towards the west is shown in yellow, towards the east in blue and dipping against ice-flow direction in light green. The dimensions of both grids are 3×3 km. Features that are aligned in flow direction that have been identified as bedforms are highlighted by yellow dashed lines in the lowest panel. Dimensions of each bedform are given in Table 1.

material area in Grid Tiger show stronger reflectivity (~ 0.7), compared to the surrounding material (~ 0.4). No clear change in reflectivity is visible between bedforms up- and downstream of the interruption of Grid Zebra. Bedforms (Bu1–5) upstream of the boundary in Grid Tiger show a weaker reflectivity (~ 1) compared to bedforms in Grid Zebra (> 1.5). The reflectivity of

the SSR is comparable to the reflectivity of bedforms in Grid Zebra.

Glaciological factors

Figure 9 shows a comparison of bed elevation, surface ice-flow speed (Gardner *et al.* 2019) and slope (Howat

Table 1. Bedform dimensions for Grids Tiger and Zebra.

Zebra			Tiger		
Name	Width (m)	Height (m)	Name	Width (m)	Height (m)
Continuous bedforms			Bedforms upstream of the boundary		
Bc1	130–250	17	Bu1	180	10
Bc2	75–95	2	Bu2	300	12
Bc3	175–230	15	Bu3	280	5
Bc4	95–125	3	Bu4	100	3
Bc5	160–190	8	Bu5	110	3
Bc6	170–180	6	Bc1 - SSR	400–550	35–50
Interrupted bedforms			Bedforms downstream of the boundary		
Bi1	105	4–6	Bd1	110	2
Bi2	85	4	Bd2	150	4
Bi3	45–65	2–3	Bd3	75	2
Bi4	40	1	Bd4	120	4
Bi5	120	4	Bd5	75	2
Bi6	50–65	1	Bd6	60	1
Bi7	95	2	Bd7	65	1
Bi8	75	2	Bd8	110	2
Bi9	105	4	Bd9	95	3
Bi10	85–100	3–5			

et al. 2022; tabulated in Table S1) in the area and the surroundings of Grids Tiger (yellow) and Zebra (green). Variations in bed elevation (Fig. 9A) and surface flow speed (Fig. 9B) are similar in both grids. The surface slope (Fig. 9C) in these areas is low: 0.24° and 0.14° in Grid Zebra and Tiger, respectively, dipping roughly in the same direction (~305°).

Sediment discharge

Figure 10 shows estimated sediment discharge for a range of effective pressures and sliding speeds, with $C_t = 1.1 \times 10^{-11}$ (s m² kg⁻¹) (representative of till with large clasts). At low N values (Fig. 10A), u_t is small and thus the sediment begins to deform at low u_b (<20 m a⁻¹) rendering the nonmonotonic relationship of utmost importance in setting Q . At high N values (Fig. 10B), u_t is larger, hence a larger u_b (>60 m a⁻¹) is required to initiate bed deformation; however, once deformation is initiated, the nonmonotonic dependence of Q on N is insignificant and Q scales proportionally with N and u_b .

The range of Q values generated for the range of N values measured in Smith *et al.* (2021) is shown in Fig. 11 for $C_t = 6.2 \times 10^{-11}$ (s m² kg⁻¹). This C_t was chosen for RIS as the sediments are likely devoid of large clasts and are composed of fine-grained sediment. For a sliding speed of ~380 m a⁻¹ (marked by the yellow line), the higher N values (204 kPa) measured at the downstream portion of Grid Tiger would inhibit sediment discharge ($Q = 0$). By contrast, at the upstream end of Grid Tiger, where lower N values were measured (168 kPa), sediment discharge could occur ($Q \sim 0.3$ m³ a⁻¹) all at the same u_b . The prediction by this model of

a transition from deforming to nondeforming conditions between the upstream and downstream ends of Grid Tiger, as a result of spatial variations in N , agrees with inferences made from previous geophysical observations (e.g. Smith 1997; King *et al.* 2009; Smith & Murray 2009) and those presented here.

Linking subglacial landscape, basal conditions and bed properties

The bed beneath RIS contains bedforms of various widths, lengths and heights. In some areas, particularly in Grid Zebra, bedform dimensions are consistent; elsewhere, particularly in Grid Tiger, they vary across and along the flow. Importantly, bedforms in both grids terminate in areas of abrupt topographic change along ice flow. Our 3D radar approach reveals, for the first time, that downstream ends of bedforms at this topographic step are distinct and characterized by a continuous depression around them. We interpret the abrupt topographic step to cause the termination or interruption of bedforms. Despite the topographic step being comparable in steepness and height (Figs 6, 8) between the two grids, Grid Tiger shows significant variation in bedform dimensions between bedforms up- and downstream of the step, whereas they are indistinguishable within Grid Zebra. Therefore, we assume other factors to be the first-order controls on variations in bedform dimensions.

Glaciological factors – ice surface slope, flow speed and topographic relief

We observe no significant difference in ice surface slope, flow speed and topographic relief between or within the two grids (Fig. 9). Given the proximity of the two grids, we assume the area to have been overridden by ice for the same duration. We, therefore, consider these glaciological parameters not to have a major influence on bedform length in this region, and length variation not to be a ‘velocity duration product’ as proposed in Clark (1993) and shown in Zoet *et al.* (2021) for geologically homogeneous regions.

Geological factors – variation in sediment discharge

Bed reflectivity indicates that bedforms in Grid Zebra are composed of soft sediment (porosity range 30–50%), with no measurable difference in sediment properties between bedforms up- and downstream of the interruption. Bedforms upstream of the boundary in Grid Tiger also consist of soft material. Bedforms downstream of the boundary show a reflectivity value that is at the hard/soft bed transition. However, their height (1–4 m) is less than the quarter wavelength (12 m for a 3.5-MHz wavelet and 0.168 m ns⁻¹ speed in ice) of the radar data, and consequently, reflectivity might be decreased from interference with the underlying

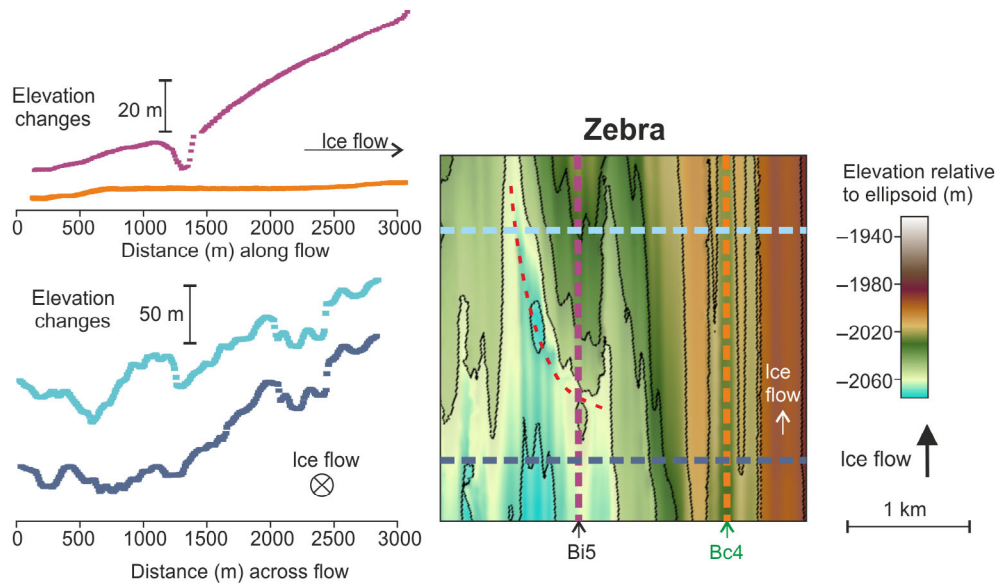


Fig. 6. Cross-sections of basal topography in Grid Zebra. See Fig. S2 for radargrams across flow. Plots on the left do not include a vertical axis showing absolute elevation, as profiles have been shifted vertically for illustrative reasons. A vertical scale bar is given in the plot.

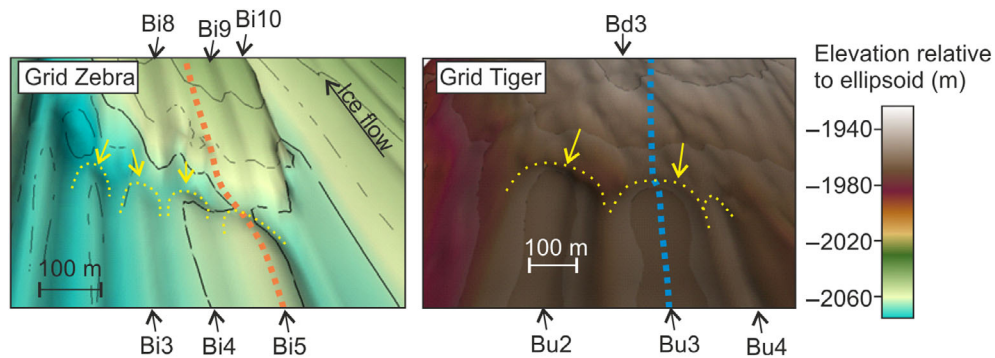


Fig. 7. Zoom on bed elevation around bedform ends.

material (Bradford & Deeds 2006). Without directly probing the sediment of the bedforms, we cannot identify changes in the granularity or hydraulic properties of the material, which might influence bedform shapes (Menzies 1979; Piotrowski 1987). Based on the reflectivity analysis we assume all bedforms, including these small bedforms in Grid Zebra, to be composed of soft sediment.

Reflectivity analysis implies the area surrounding small bedforms downstream of the boundary at Grid Tiger is composed of low-porosity material (Fig. 5H) whereas bed material upstream of the boundary at Grid Tiger has higher porosity. A lower porosity material, and presumably less deformation of sediment in this area, agrees with the rougher appearance of the topography downstream of the boundary (visible as more undulation in the basal topography shown in purple in Fig. 8), compared to the soft bed in Grid Zebra (visible as less undulation in the basal topography shown in purple in Fig. 6).

The proposed relationship for evaluating sediment deformation (Eqn. 1) suggests that small but significant spatial variations in N can explain the observed geophysical variations. In areas where the bed has a lower N value (like the upstream portion of Grid Tiger), and thus lower u_b , deformation of the bed is more likely to occur at the u_b values found for RIS (e.g. Fig. 11). Such an actively deforming bed will cause the sediment to dilate and reach its critical state porosity. In these locations, basal motion will be largely facilitated by deformation of the sediment. Conversely, areas with elevated N values (like downstream of the boundary in Grid Tiger), and thus a higher u_b , may undergo little to no bed deformation. Here deformation of the sediment will not occur and sediments will consolidate. Because sediment consolidation is proportional to the imposed N at the base, sediments in Grid Tiger downstream of the boundary should have lower porosities, as observed in the geophysical observations. Variations in N over these relatively short spatial

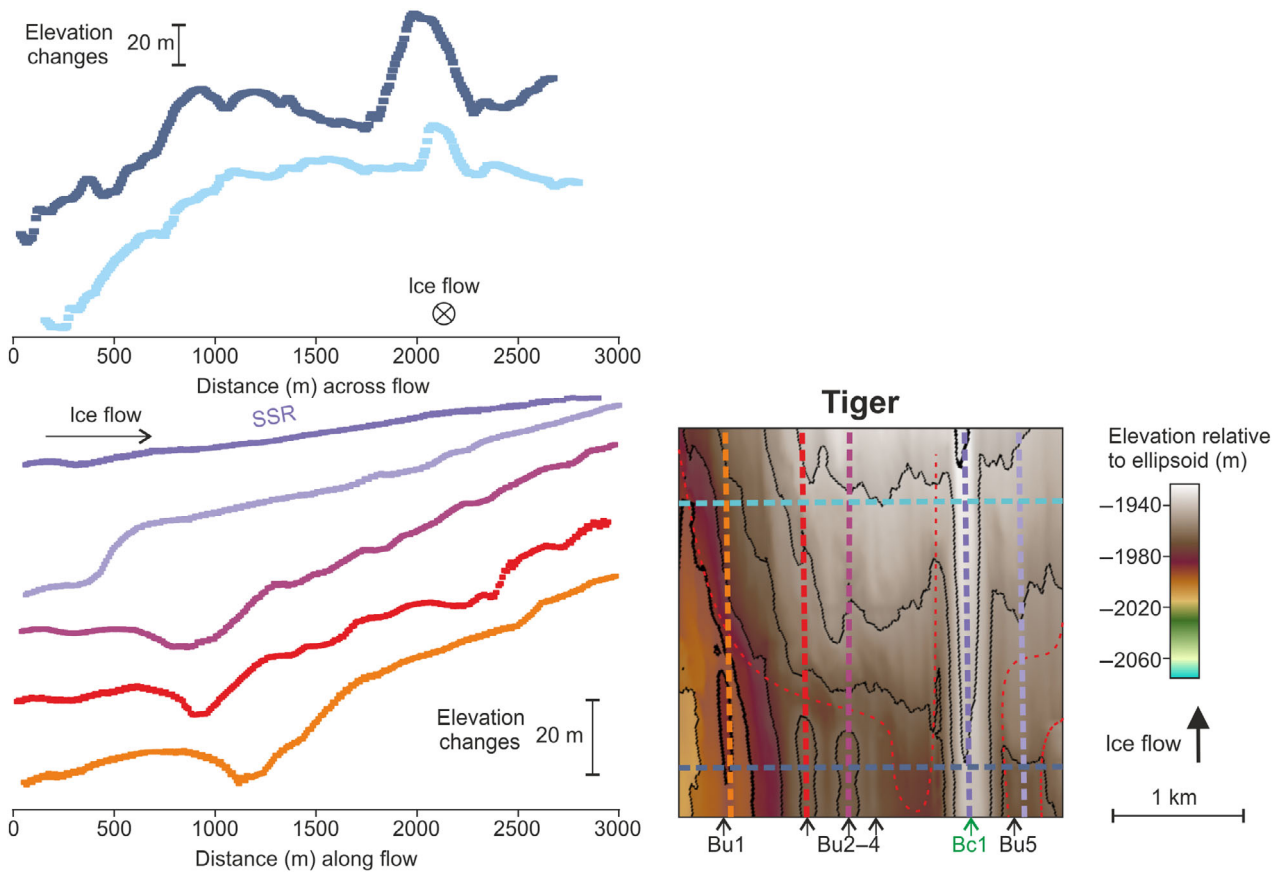


Fig. 8. Cross-sections of basal topography in Grid Tiger. See Figs S2 and S3 for radargrams across flow. Plots on the left do not include a vertical axis showing absolute elevation, as profiles have been shifted vertically for illustrative reasons. A vertical scale bar is given in the plot.

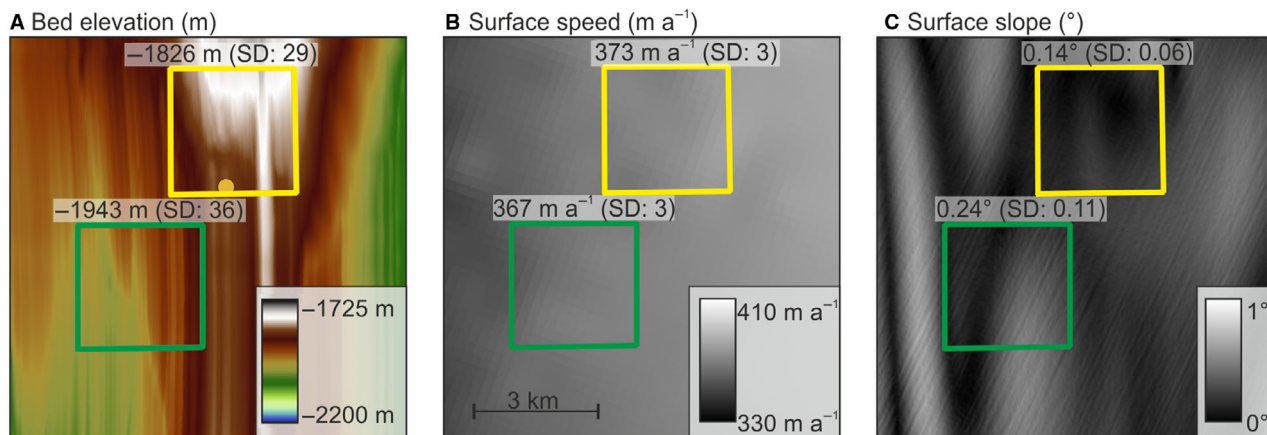


Fig. 9. Comparison of different properties in the area and surroundings of Grid Zebra and Grid Tiger: A. Bed elevation, B. Surface flow speed at 240-m resolution (Gardner *et al.* 2019) and C. Surface slope with a horizontal resolution of 2 m (Howat *et al.* 2022). The mean, standard deviation and minimum and maximum values for each grid are given in Table S1.

scales could result from spatial variability in hydraulic permeability of the sediment due to small variations in grain-size distributions (e.g. Boulton 1987).

The role of N becomes important in shaping RIS bed-forms due to its effect on sediment discharge (Eqn. 4).

Downstream of the boundary in Grid Tiger, higher N values (204 kPa) inhibit sediment deformation ($Q = 0$; Fig. 11), whereas at the upstream end of Grid Tiger, where lower N values were measured (168 kPa), sediment deformation could occur ($Q \sim 0.3 \text{ m}^3 \text{ a}^{-1}$, Fig. 11), all at

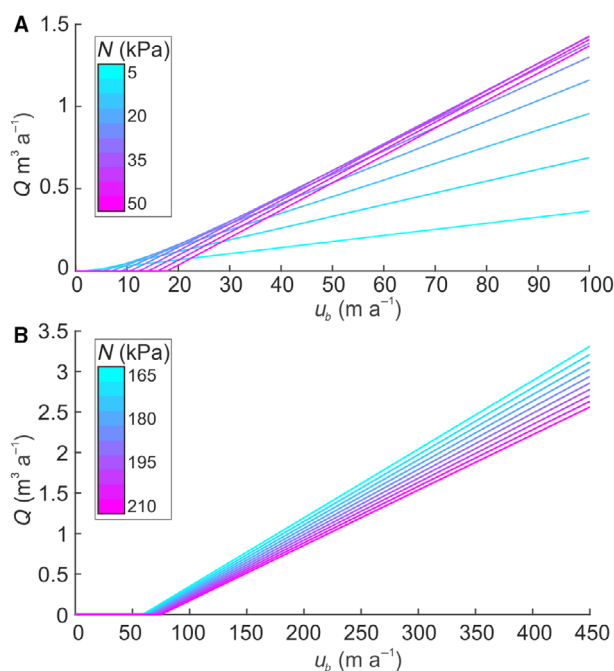


Fig. 10. Q estimates from Equation 4 with different N values and $C_t = 1.1 \times 10^{-11}$ ($\text{s m}^2 \text{kg}^{-1}$). A. Shows low N values where the non-monotonic response tends to dominate. B. Shows the role of N on u_b in determining the Q response.

the same u_b of 380 m a^{-1} . In the upstream portion, where we find soft sediment, sediment discharge is high resulting in longer bedforms whereas downstream of the boundary, in the area of low-porosity material, where Q decreases (and likely ceases), bedforms are smaller. In Grid Zebra, where conditions are more homogenous and suggest higher porosities (Fig. 5), all areas are likely deforming and conducive to sediment discharge and thus bedforms are generally similar up- and downstream of the interruption.

Importance of new insights

Small bedforms in Grid Tiger appear to consist of soft material, while surrounded by low-porosity material, implying that the soft sediment has been deposited on low-porosity material. Currently, only a few numerical models of bedform formation (e.g. Barchyn *et al.* 2016) are able to explain the formation of soft bedforms on a hard bed, possibly as, to date, evidence for their existence was lacking.

Effective pressure, the granularity and hydraulic properties of the sediment, and the coupling at the ice-bed interface are the factors influencing the subglacial sediment discharge (e.g. Damsgaard *et al.* 2020; Hansen & Zoet 2022) and beneath RIS spatial variability of the sediment discharge is reflected in the spatial variability of bedform dimensions. This observation of bedform dimension variation with varying basal properties agrees with observations in the palaeo-record (e.g. Rattas &

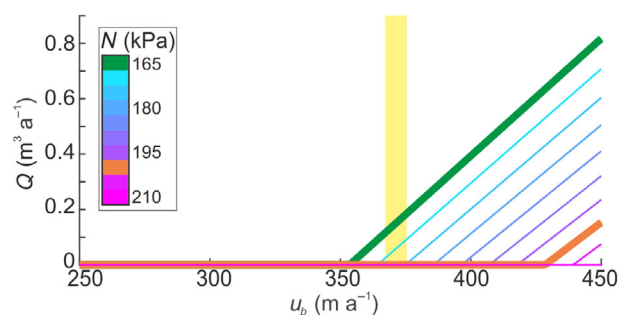


Fig. 11. Here N values spanning those found in Smith *et al.* (2021) were used along with a $C_t = 6.2 \times 10^{-11}$ ($\text{s m}^2 \text{kg}^{-1}$) value that represents fine-grained sediment devoid of large clasts. Yellow band indicates measured ice-flow speed.

Piotrowski 2003; Greenwood & Clark 2010; Phillips *et al.* 2010; V erit e *et al.* 2024). V erit e *et al.* (2024) analysed spatial variation in bedform appearance in the palaeo-record and concluded that if bedforms are produced by the same physical process and glaciological factors are constant, spatial variation in bedform dimension and orientation can be used to map spatial variation in boundary conditions, such as the basal properties. The study presented here validates this assumption, by imaging these spatial variations in bedform dimensions beneath a modern ice stream. We further found variation in basal properties and effective pressure to be the first-order controls on bedform dimensions using a sediment discharge model.

Zoet & Iverson (2020) showed that a regularized Coulomb slip response is appropriate for sediment beds and that in the areas where the bed is ‘hard’ and non-deforming, drag will occur through a rate strengthening slip response whereas in areas where the bed is ‘soft’ (i.e. deforming) drag occurs in accordance with the Coulomb nature of the till. In this manner, by separating the sections of the bed into ‘hard’ or ‘soft’ using the radar reflectivity and the bedform dimensions (e.g. Fig. 6), it is possible to designate where the regularized Coulomb slip response is rate strengthening and where it is Coulomb. For example, our radar observations in combination with Equation 1 predict that the dominant mechanisms of ice movement in Grid Zebra and Grid Tiger upstream of the boundary is slip via bed deformation (Coulomb) whereas in Grid Tiger downstream of the boundary slip is via basal sliding (rate strengthening). The interpretations from Smith (1997) and Smith & Murray (2009) regarding this change in the dominant slip mechanism appear to be in agreement with the quantitative prediction from our model. The consistency between our model and the available observations open up the future possibility of using Zoet & Iverson (2020)’s Equation 3 with measured N values from RIS to estimate values of basal drag. Comparison with basal drag values from surface inversions could provide a path towards validating ice flow models while creating more physically based models of ice flow.

Observations here imply that variations in basal sediment discharge cannot be assumed to be constant within a flowset (Stokes & Clark 2002). Previous studies reported that such spots of higher basal drag, also referred to as till-free spots, can have a major impact on ice flow and a till-free interface existing over larger areas can cause the frictional shut-down of ice streams (Stokes & Clark 2001). However, in this study, we identify small bedforms composed of soft sediment deposited in an area of low-porosity material. These small bedforms represent variations in basal properties and basal topography, which might modify basal drag (King *et al.* 2009). The interplay of bedform deposition with variations in basal drag could promote further feedback effects, which cause bedforms to gain in size and further modify the basal drag and thus influence the glacial force balance (Gudmundsson 1997; Schoof 2002).

Conclusions

Combining different imaging approaches and high-resolution 3D radar data we mapped dimensions of subglacial bedforms more accurately than was previously possible, especially bedform length and ends (upstream and downstream), and were able to identify and determine the shape of the smallest features (<300 m length, previously completely unidentifiable). We found areas where bedform dimensions remain constant along and across the flow, whereas in other areas bedforms vary. We thus developed a simple model relating sediment discharge (and hence, deformation) to basal conditions and applied it to our observations, combined with available measurements of basal effective pressure. The model implies that effective pressure and sediment properties (low-porosity material vs. soft sediment) at the ice-bed interface are first-order controls on sediment discharge and thus bedform dimensions and hence, the resulting subglacial landscape. It is interesting to note that a relatively small change in effective pressure (40 kPa) in this case correlates with a significant change in basal processes. In the area of elevated basal effective pressure, and low sediment discharge, the dominant slip mechanism is basal sliding, whereas in the area of lower effective pressure, and thus higher sediment discharge, we find basal deformation of the soft sediment to be the dominant mechanism of ice flow. This transition of slip mechanism is consistent with the pattern of located ice quakes at the ice-bed interface (Kufner *et al.* 2021). Assuming glaciological factors to be constant in the region investigated, the approach applied here allows spatial variation in basal conditions and effective pressure to be identified from spatial variation in bedform dimensions, and thus the flow mechanism to be separated into basal slip and basal deformation.

Numerical models of ice-flow dynamics require improved information on basal conditions and processes, and about their variations. Our rigorous 3D approach to ground-based radar data acquisition, processing and anal-

ysis gives significant improvements over traditional methods in the ability to map and interpret basal conditions. The consistency between our data, albeit limited, and a simple sediment discharge model is a further step towards an improved understanding of basal processes and their successful incorporation into ice-flow models. Incorporating the insights from this study into ice-flow models would require u_b , N and sediment properties to be known. Numerical ice-flow models usually include information about u_b and N ; hence, only an estimation of sediment properties, which can be achieved from geophysical methods, analogue lab experiments or possibly discrete element method modelling, is required. We strongly encourage more data acquisition of this nature (and comparable airborne radar swath data; e.g. Holschuh *et al.* 2020) as well as more, relevant observations to test and develop further the sediment discharge model.

Acknowledgements. – This work was funded by NERC award numbers NE/G014159/1, NE/G013187/1 and NE/F015879/1, and NERC National Capability Science: Strategic Research and Innovation Short Projects. LKZ was supported by NSF OPP award number 2048315. Geophysical equipment was provided by NERC's Geophysical Equipment Facility, loan number 887. We thank BAS Operations for their fieldwork support and B. Craven for their software support. University of Leeds acknowledges support of this work by Landmark Software and Services, a Landmark Company and use of SeisSpace/ProMAX via the Landmark University Grant Program, Agreements 2004-COM-024982, 2008-CON-010888 and subsequent renewals. SLB is thanked for supplying educational licences for its Petrel software. We acknowledge support by Open Access Publishing Fund of University of Tübingen. We further thank the Editor Jan A. Piotrowski, Chris Stokes and one anonymous reviewer for helpful comments that greatly improved the clarity of the manuscript. Open Access funding enabled and organized by Projekt DEAL.

Author contributions. – RS: data curation; investigation; methodology; visualization; writing – original draft; writing – review and editing. LKZ: data curation, investigation; methodology; visualization; writing – original draft; writing – review and editing. ADB: investigation; methodology; writing – review and editing. AMS: data curation, investigation; methodology; writing – review and editing funding acquisition; project administration. RAC: investigation; methodology; writing – review and editing. AMB: investigation; methodology; writing – review and editing.

Data availability statement. – Topography and reflectivity from 3D migrated radar data are archived and available via the UK Polar Data Center: <https://doi.org/10.5285/dbf2e081-b332-4d20-b242-2daa5fed25ae>.

References

- Ashmore, D. W. & Bingham, R. G. 2014: Antarctic subglacial hydrology: current knowledge and future challenges. *Antarctic Science* 26, 758–773. <https://doi.org/10.1017/S0954102014000546>.
- Bamber, J. L., Oppenheimer, M., Kopp, R. E., Aspinall, W. P. & Cooke, R. M. 2019: Ice sheet contributions to future sea-level rise from structured expert judgment. *Proceedings of the National Academy of Sciences of the United States of America* 166, 11195–11200. <https://doi.org/10.1073/pnas.1817205116>.
- Barchyn, T. E., Dowling, T. P. F., Stokes, C. R. & Hugenholtz, C. H. 2016: Subglacial bed form morphology controlled by ice speed and sediment thickness. *Geophysical Research Letters* 43, 7572–7580. <https://doi.org/10.1002/2016GL069558>.

- Bindschadler, R., Choi, H., Wichlacz, A., Bingham, R., Bohlander, J., Brunt, K., Corr, H., Drews, R., Fricker, H., Hall, M., Hindmarsh, R., Kohler, J., Padman, L., Rack, W., Rotschky, G., Urbini, S., Vornerberger, P. & Young, N. 2011: Getting around Antarctica: new high-resolution mappings of the grounded and freely-floating boundaries of the Antarctic ice sheet created for the International Polar Year. *The Cryosphere* 5, 569–588. <https://doi.org/10.5194/tc-5-569-2011>.
- Bingham, R. G., Vaughan, D. G., King, E. C., Davies, D., Cornford, S. L., Smith, A. M., Arthern, R. J., Brisbourne, A. M., De Rydt, J., Graham, A. G. C., Spagnolo, M., Marsh, O. J. & Shean, D. E. 2017: Diverse landscapes beneath Pine Island Glacier influence ice flow. *Nature Communications* 8, 1618. <https://doi.org/10.1038/s41467-017-01597-y>.
- Booth, A. D., Linford, N. T., Clark, R. A. & Murray, T. 2008: Three-dimensional, multi-offset ground-penetrating radar imaging of archaeological targets. *Archaeological Prospection* 15, 93–112. <https://doi.org/10.1002/arp.327>.
- Boulton, G. S. 1987: A theory of drumlin formation by subglacial sediment deformation. In Rose, J. & Menzies, J. (eds.): *Drumlin symposium*, 25–80. Balkema, Rotterdam.
- Bradford, J. H. & Deeds, J. C. 2006: Ground-penetrating radar theory and application of thin-bed offset-dependent reflectivity. *Geophysics* 71, K47–K57. <https://doi.org/10.1190/1.2194524>.
- Brondex, J., Gillet-Chaulet, F. & Gagliardini, O. 2019: Sensitivity of centennial mass loss projections of the Amundsen basin to the friction law. *The Cryosphere* 13, 177–195. <https://doi.org/10.5194/tc-13-177-2019>.
- Carter, S. P., Blankenship, D. D., Peters, M. E., Young, D. A., Holt, J. W. & Morse, D. L. 2007: Radar-based subglacial lake classification in Antarctica. *Geochemistry, Geophysics, Geosystems* 8, Q03016. <https://doi.org/10.1029/2006GC001408>.
- Chopra, S. & Marfurt, K. J. 2005: Seismic attributes – a historical perspective. *Geophysics* 70, 350–2850. <https://doi.org/10.1190/1.2098670>.
- Chopra, S. & Marfurt, K. J. 2007: Seismic Attributes for Prospect Identification and Reservoir Characterization. *Geophysical Development Series* 11, 465. <https://doi.org/10.1190/1.9781560801900>.
- Chu, W., Creyts, T. T. & Bell, R. E. 2016: Rerouting of subglacial water flow between neighboring glaciers in West Greenland. *Journal of Geophysical Research: Earth Surface* 121, 925–938. <https://doi.org/10.1002/2015JF003705>.
- Clark, C. D. 1993: Mega-scale glacial lineations and cross-cutting ice-flow landforms. *Earth Surface Processes and Landforms* 18, 1–29. <https://doi.org/10.1002/esp.3290180102>.
- Clark, C. D., Ely, J. C., Spagnolo, M., Hahn, U., Hughes, A. L. C. & Stokes, C. R. 2018: Spatial organization of drumlins. *Earth Surface Processes and Landforms* 43, 499–513. <https://doi.org/10.1002/esp.4192>.
- Clyne, E. R., Anandakrishnan, S., Muto, A., Alley, R. B. & Voigt, D. E. 2020: Interpretation of topography and bed properties beneath Thwaites Glacier, West Antarctica using seismic reflection methods. *Earth and Planetary Science Letters* 550, 116543. <https://doi.org/10.1016/j.epsl.2020.116543>.
- Corr, H. 2020: Airborne radar bed elevation along flow lines covering the Evans, and Rutford Ice Streams, and ice rises in the Ronne Ice Shelf (2006/07) (Version 1.0) [Data set]. UK Polar Data Centre, Natural Environment Research Council, UK Research & Innovation. <https://doi.org/10.5285/4efa688e-7659-4cbf-a72f-facac5d63998>.
- Damsgaard, A., Goren, L. & Suckale, J. 2020: Water pressure fluctuations control variability in sediment flux and slip dynamics beneath glaciers and ice streams. *Communications Earth & Environment* 1, 66. <https://doi.org/10.1038/s43247-020-00074-7>.
- Delf, R., Schroeder, D. M., Curtis, A., Giannopoulos, A. & Bingham, R. G. 2020: A comparison of automated approaches to extracting englacial-layer geometry from radar data across ice sheets. *Annals of Glaciology* 61, 234–241. <https://doi.org/10.1017/aog.2020.42>.
- Doake, C. S. M., Frolich, R. M., Mantripp, D. R., Smith, A. M. & Vaughan, D. G. 1987: Glaciological studies on Rutford Ice Stream, Antarctica. *Journal of Geophysical Research* 92, 8951–8960. <https://doi.org/10.1029/JB092iB09p08951>.
- Finlayson, A., Phillips, E., Benediktsson, Í. Ó., Zoet, L. K., Iverson, N. R. & Everest, J. 2019: Subglacial drumlins and englacial fractures at the surge-type glacier, Múlajökull, Iceland. *Earth Surface Processes and Landforms* 44, 367–380. <https://doi.org/10.1002/esp.4485>.
- Fox-Kemper, B., Hewitt, H. T., Xiao, C., Aþalgeirsdóttir, G., Drijfhout, S. S., Edwards, T. L., Gollledge, N. R., Hemer, M., Kopp, R. E., Krinner, G., Mix, A., Notz, D., Nowicki, S., Nurhati, I. S., Ruiz, L., Sallée, J.-B., Slangen, A. B. A. & Yu, Y. 2023: Ocean, cryosphere and sea level change. In Masson-Delmotte, V., Zhai, P., Pirani, A., Connors, S. L., Péan, C., Berger, S., Caud, N., Chen, Y., Goldfarb, L., Gomis, M. I., Huang, M., Leitzell, K., Lonnoy, E., Matthews, J. B. R., Maycock, T. K., Waterfield, T., Yelekçi, O. & Yu, R. B. Z. (eds.): *Climate Change 2021, The Physical Science Basis. Contribution of Working Group I to the Sixth Assessment Report of the Intergovernmental Panel on Climate Change*, 1211–1362. Cambridge University Press, Cambridge. <https://doi.org/10.1017/9781009157896.011>.
- Gardner, A. S., Fahnestock, M. A. & Scambos, T. A. 2019: ITS_LIVE regional glacier and ice sheet surface velocities: version 1. Data archived at National Snow and Ice Data Center. <https://doi.org/10.5067/6II6VW8LLWJ7>.
- Gardner, A. S., Moholdt, G., Scambos, T., Fahnestock, M., Ligtenberg, S., van den Broeke, M. & Nilsson, J. 2018: Increased West Antarctic and unchanged East Antarctic ice discharge over the last 7 years. *The Cryosphere* 12, 521–547. <https://doi.org/10.5194/tc-12-521-2018>.
- Gillet-Chaulet, F., Durand, G., Gagliardini, O., Mosbeux, C., Mouginot, J., Rémy, F. & Ritz, C. 2016: Assimilation of surface velocities acquired between 1996 and 2010 to constrain the form of the basal friction law under Pine Island Glacier. *Geophysical Research Letters* 43(10), 10,311–10,321. <https://doi.org/10.1002/2016GL069937>.
- Grasmueck, M., Weger, R. & Horstmeyer, H. 2005: Full-resolution 3D GPR imaging. *Geophysics* 70, K12–K19. <https://doi.org/10.1190/1.1852780>.
- Greenwood, S. L. & Clark, C. D. 2010: The sensitivity of subglacial bedform size and distribution to substrate lithological control. *Sedimentary Geology* 232, 130–144. <https://doi.org/10.1016/j.sedgeo.2010.01.009>.
- Gudmundsson, G. H. 1997: Basal-flow characteristics of a non-linear flow sliding frictionless over strongly undulating bedrock. *Journal of Glaciology* 43, 80–89. <https://doi.org/10.3189/S0022143000002835>.
- Hansen, D. D. & Zoet, L. K. 2022: Characterizing sediment flux of deforming glacier beds. *Journal of Geophysical Research: Earth Surface* 127, e2021JF006544. <https://doi.org/10.1029/2021JF006544>.
- Holschuh, N., Christianson, K., Paden, J., Alley, R. B. & Anandakrishnan, S. 2020: Linking postglacial landscapes to glacier dynamics using swath radar at Thwaites Glacier, Antarctica. *Geology* 48, 268–272. <https://doi.org/10.1130/G46772.1>.
- Howat, I., Porter, C., Noh, M.-J., Husby, E., Khuvis, S., Danish, E., Tomko, K., Gardiner, J., Negrete, A., Yadav, B., Klassen, J., Kelleher, C., Cloutier, M., Bakker, J., Enos, J., Arnold, G., Bauer, G. & Morin, P. 2022: The reference elevation model of Antarctica – Mosaics, Version 2, Harvard Dataverse. <https://doi.org/10.7910/DVN/EBW8UC>.
- Hudson, T. S., Kufner, S. K., Brisbourne, A. M., Kendall, J. M., Smith, A. M., Alley, R. B., Arthern, R. J. & Murray, T. 2023: Highly variable friction and slip observed at Antarctic ice stream bed. *Nature Geoscience* 16, 612–618. <https://doi.org/10.1038/s41561-023-01204-4>.
- Johnson, M. D., Schomacker, A., Benediktsson, Í. Ó., Geiger, A. J., Ferguson, A. & Ingólfsson, Ó. 2010: Active drumlin field revealed at the margin of Múlajökull, Iceland: a surge-type glacier. *Geology* 38, 943–946. <https://doi.org/10.1130/G31371.1>.
- Joughin, I., Smith, B. E. & Schoof, C. G. 2019: Regularized Coulomb Friction Laws for Ice Sheet Sliding: application to Pine Island Glacier, Antarctica. *Geophysical Research Letters* 46, 4764–4771. <https://doi.org/10.1029/2019GL082526>.
- King, E. C. 2020: The precision of radar-derived subglacial bed topography: a case study from Pine Island Glacier, Antarctica. *Annals of Glaciology* 61, 154–161. <https://doi.org/10.1017/aog.2020.33>.
- King, E. C., Hindmarsh, R. C. A. & Stokes, C. R. 2009: Formation of mega-scale glacial lineations observed beneath a West Antarctic ice stream. *Nature Geoscience* 2, 585–588. <https://doi.org/10.1038/ngeo581>.
- King, E. C., Pritchard, H. D. & Smith, A. M. 2016: Subglacial landforms beneath Rutford Ice Stream, Antarctica: detailed bed topography from ice-penetrating radar. *Earth System Science Data* 8, 151–158. <https://doi.org/10.5194/essd-8-151-2016>.
- King, E. C., Woodward, J. & Smith, A. M. 2007: Seismic and radar observations of subglacial bedforms beneath the onset zone of Rutford Ice Stream, Antarctica. *Journal of Glaciology* 53, 665–672. <https://doi.org/10.3189/002214307784409216>.

- Koyan, P., Tronicke, J. & Allroggen, N. 2021: 3D ground-penetrating radar attributes to generate classified facies models: a case study from a dune Island. *Geophysics* 86, B335–B347. <https://doi.org/10.1190/geo2021-0204.1>.
- Kufner, S.-K., Brisbane, A. M., Smith, A. M., Hudson, T. S., Murray, T., Schlegel, R., Kendall, J. M., Anandakrishnan, S. & Lee, I. 2021: Not all Icequakes are created equal: basal Icequakes suggest diverse bed deformation mechanisms at Rutford Ice Stream, West Antarctica. *Journal of Geophysical Research: Earth Surface* 126(3), e2020JF006001. <https://doi.org/10.1029/2020JF006001>.
- Menzies, J. 1979: The mechanics of Drumlin formation with particular reference to the change in pore-water content of the till. *Journal of Glaciology* 22, 373–384. <https://doi.org/10.1017/S0022143000014349>.
- Mohebian, R., Riahi, M. A. & Yousefi, O. 2018: Detection of channel by seismic texture analysis using Grey Level Co-occurrence Matrix based attributes. *Journal of Geophysics and Engineering* 15, 1953–1962. <https://doi.org/10.1088/1742-2140/aac099>.
- Murray, T., Corr, H., Forieri, A. & Smith, A. M. 2008: Contrasts in hydrology between regions of basal deformation and sliding beneath Rutford Ice Stream, West Antarctica, mapped using radar and seismic data. *Geophysical Research Letters* 35, L12504. <https://doi.org/10.1029/2008GL033681>.
- Murray, T., Smith, A. M., King, M. A. & Weedon, G. P. 2007: Ice flow modulated by tides at up to annual periods at Rutford Ice Stream, West Antarctica. *Geophysical Research Letters* 34, L18503. <https://doi.org/10.1029/2007GL031207>.
- Nias, I. J., Cornford, S. L. & Payne, A. J. 2018: New mass-conserving bedrock topography for Pine Island glacier impacts simulated decadal rates of mass loss. *Geophysical Research Letters* 45, 3173–3181. <https://doi.org/10.1002/2017GL076493>.
- Phillips, E., Everest, J. & Diaz-Doce, D. 2010: Bedrock controls on subglacial landform distribution and geomorphological processes: evidence from the Late Devensian Irish Sea Ice Stream. *Sedimentary Geology* 232, 98–118. <https://doi.org/10.1016/j.sedgeo.2009.11.004>.
- Piotrowski, J. A. 1987: Genesis of the Woodstock drumlin field, southern Ontario, Canada. *Boreas* 16, 249–265. <https://doi.org/10.1111/j.1502-3885.1987.tb00094.x>.
- Rattas, M. & Piotrowski, J. A. 2003: Influence of bedrock permeability and till grain size on the formation of the saadjärve drumlin field, Estonia, under an east-Baltic Weichselian ice stream. *Boreas* 32, 167–177. <https://doi.org/10.1080/03009480310001849>.
- Ritz, C., Edwards, T. L., Durand, G., Payne, A. J., Peyaud, V. & Hindmarsh, R. C. A. 2015: Potential sea-level rise from Antarctic ice-sheet instability constrained by observations. *Nature* 528, 115–118. <https://doi.org/10.1038/nature16147>.
- Schlegel, R., Brisbane, A. M., Smith, A. M., Booth, A. D., Murray, T., King, E. C. & Clark, R. A. 2024: Subglacial bedform and moat initiation beneath Rutford Ice Stream, West Antarctica. *Geomorphology* 458, 109207. <https://doi.org/10.1016/j.geomorph.2024.109207>.
- Schlegel, R., Murray, T., Smith, A. M., Brisbane, A. M., Booth, A. D., King, E. C. & Clark, R. A. 2022: Radar derived subglacial properties and landforms beneath Rutford Ice Stream, West Antarctica. *Journal of Geophysical Research: Earth Surface* 127, e2021JF006349. <https://doi.org/10.1029/2021JF006349>.
- Schoof, C. 2002: Basal perturbations under ice streams: form drag and surface expression. *Journal of Glaciology* 48, 407–416. <https://doi.org/10.3189/172756502781831269>.
- Siegert, M. J. & Ridley, J. K. 1998: Determining basal ice-sheet conditions in the Dome C region of East Antarctica using satellite radar altimetry and airborne radio-echo sounding. *Journal of Glaciology* 44, 1–8. <https://doi.org/10.3189/S002214300000229X>.
- Smith, A. M. 1997: Basal conditions on Rutford Ice Stream, West Antarctica, from seismic observations. *Journal of Geophysical Research* 102, 543–552.
- Smith, A. M. & Murray, T. 2009: Bedform topography and basal conditions beneath a fast-flowing West Antarctic ice stream. *Quaternary Science Reviews* 28, 584–596. <https://doi.org/10.1016/j.quascirev.2008.05.010>.
- Smith, A. M., Anker, P. G. D., Nicholls, K. W., Makinson, K., Murray, T., Rios-Costas, S., Brisbane, A. M., Hodgson, D. A., Schlegel, R. & Anandakrishnan, S. 2021: Ice stream subglacial access for ice-sheet history and fast ice flow: the BEAMISH Project on Rutford Ice Stream, West Antarctica and initial results on basal conditions. *Annals of Glaciology* 62, 203–211. <https://doi.org/10.1017/aog.2020.82>.
- Smith, A. M., Murray, T., Nicholls, K. W., Makinson, K., Adalgeirsdóttir, G., Behar, A. E. & Vaughan, D. G. 2007: Rapid erosion, drumlin formation, and changing hydrology beneath an Antarctic ice stream. *Geology* 35, 127–130. <https://doi.org/10.1130/G23036A.1>.
- Spagnolo, M., Clark, C. D., Ely, J. C., Stokes, C. R., Anderson, J. B., Andreassen, K., Graham, A. G. C. & King, E. C. 2014: Size, shape and spatial arrangement of mega-scale glacial lineations from a large and diverse dataset. *Earth Surface Processes and Landforms* 39, 1432–1448. <https://doi.org/10.1002/esp.3532>.
- Stokes, C. R. 2018: Geomorphology under ice streams: moving from form to process. *Earth Surface Processes and Landforms* 43, 85–123. <https://doi.org/10.1002/esp.4259>.
- Stokes, C. R. & Clark, C. D. 2001: Palaeo-ice streams. *Quaternary Science Reviews* 20, 1437–1457.
- Stokes, C. R. & Clark, C. D. 2002: Are long subglacial bedforms indicative of fast ice flow? *Boreas* 31, 239–249. <https://doi.org/10.1111/j.1502-3885.2002.tb01070.x>.
- Taner, M. T. 2001: Seismic attributes. *CSEG Recorder* 26, 48–56.
- Taner, M. T., Koehler, F. & Sheriff, R. E. 1979: Complex seismic trace analysis. *Geophysics* 44, 1041. <https://doi.org/10.1190/1.1440994>.
- Tulaczyk, S., Kamb, B., Scherer, R. P. & Engelhardt, H. F. 1998: Sedimentary processes at the base of a West Antarctic ice stream: constraints from textural and compositional properties of subglacial debris. *Journal of Sedimentary Research* 68, 487–496. <https://doi.org/10.2110/jsr.68.487>.
- Vérité, J., Ravier, E., Bourgeois, O., Pochat, S. & Bessin, P. 2024: The kinematic significance of subglacial bedforms and their use in palaeo-glaciological reconstructions. *Earth and Planetary Science Letters* 626, 118510. <https://doi.org/10.1016/j.epsl.2023.118510>.
- Wright, A. P., Young, D. A., Bamber, J. L., Dowdeswell, J. A., Payne, A. J., Blankenship, D. D. & Siegert, M. J. 2014: Subglacial hydrological connectivity within the Byrd Glacier catchment, East Antarctica. *Journal of Glaciology* 60, 345–352. <https://doi.org/10.3189/2014JoG13J014>.
- Zhao, W., Forte, E., Colucci, R. R. & Pipan, M. 2016: High-resolution glacier imaging and characterization by means of GPR attribute analysis. *Geophysical Journal International* 206, 1366–1374. <https://doi.org/10.1093/gji/ggw208>.
- Zoet, L. K. & Iverson, N. R. 2020: A slip law for glaciers on deformable beds. *Science* 368, 76–78. <https://doi.org/10.1126/science.aaz1183>.
- Zoet, L. K., Rawling, J. E., Woodard, J. B., Barrette, N. & Mickelson, D. M. 2021: Factors that contribute to the elongation of drumlins beneath the Green Bay Lobe, Laurentide Ice Sheet. *Earth Surface Processes and Landforms* 46, 2540–2550. <https://doi.org/10.1002/esp.5192>.

Supporting Information

Additional Supporting Information to this article is available at <http://www.boreas.dk>.

Fig. S1. The blue dots are the Tsb data from Hansen and Zoet (2022) for varying effective pressures, N , at a velocity of 100 m a^{-1} . The orange line is the nonmonotonic fit to the data using constants of $C_1 = 1.5 \times 10^3 \text{ (kg s}^{-2}\text{)}$ and $C_2 = 2 \times 10^9 \text{ (Pa}^2\text{)}$.

Fig. S2. Radargram showing the bed reflection across flow in Grids Tiger and Zebra.

Fig. S3. Bedforms downstream of the boundary in Grid Tiger.

Table S1. Mean, standard deviation and minimum and maximum values of bed elevation, surface speed, surface slope and surface azimuth within Grid Tiger and Grid Zebra.